Nanoscale

RSC Publishing

PAPER

View Article Online
View Journal | View Issue

Cite this: *Nanoscale*, 2013, **5**, 6857

VEGF-loaded graphene oxide as theranostics for multi-modality imaging-monitored targeting therapeutic angiogenesis of ischemic muscle†

Zhongchan Sun,‡[ab] Peng Huang,‡[bc] Guang Tong,[d] Jing Lin,[bc] Albert Jin,[e] Pengfei Rong,[b] Lei Zhu,[bf] Liming Nie,[b] Gang Niu,*[b] Feng Cao*[a] and Xiaoyuan Chen*[b]

Received 30th March 2013
Accepted 15th May 2013

DOI: 10.1039/c3nr01573d

www.rsc.org/nanoscale

Herein we report the design and synthesis of multifunctional VEGF-loaded IR800-conjugated graphene oxide (GO-IR800-VEGF) for multi-modality imaging-monitored therapeutic angiogenesis of ischemic muscle. The as-prepared GO-IR800-VEGF positively targets VEGF receptors, maintains an elevated level of VEGF in ischemic tissues for a prolonged time, and finally leads to remarkable therapeutic angiogenesis of ischemic muscle. Although more efforts are required to further understand the *in vivo* behaviors and the long-term toxicology of GO, our work demonstrates the success of using GO for efficient VEGF delivery *in vivo* by intravenous administration and suggests the great promise of using graphene oxide in theranostic applications for treating ischemic disease.

1 Introduction

Peripheral vascular disease (PAD) is one of the most common vascular diseases in the world.[1] PAD mainly involves the impairment of blood flow to the extremities, resulting from common cardiovascular morbidities such as atherosclerotic occlusive disease, diabetes mellitus, hyperlipidemia and so on. In the United States, 8 million people with PAD are devastated by severe symptoms and complications such as immobility, intractable ischemia, ulceration, impaired wound healing or amputation. Only 15–20% of these patients are suitable candidates for mechanical revascularization therapies such as surgical bypass or stent implantation. For the rest of the PAD patients, the only hope of salvaging their affected limbs lies in therapeutic angiogenesis.[2–5]

Therapeutic angiogenesis, which aims to stimulate new blood vessel formation *via* the sprouting and branching of existing vessels in ischemic tissues, has received extensive attention for PAD treatment.[4–9] Successful therapeutic angiogenesis depends on (i) the targeted delivery of various growth factors such as vascular endothelial growth factor (VEGF) to ischemic tissues, and (ii) the sustained high concentration of growth factors in ischemic tissues.[10] Clinical trials of administering growth factors by either local injection into ischemic sites or intravenous injection failed to obtain a significant therapeutic effect, most likely due to the short circulation half-life and lack of specific delivery of growth factors.[11–13] Therefore, targeted delivery and sustained release of growth factors in ischemic sites is a grand challenge.

Inspired by the targeted drug delivery for tumor therapy using nanocarriers, some efforts have been made towards the targeted delivery of VEGF to ischemic sites.[4,8,10] Nanocarriers as novel delivery systems show the following features: (i) nanocarriers have long circulation in the bloodstream and rapidly permeate biobarriers such as cell membranes and fenestrated vasculatures.[14,15] (ii) Nanocarriers can easily enter a leaky angiogenic endothelium, thus providing some specificity, namely enhanced permeability and retention (EPR) effect.[16] (iii) Nanocarriers display low osmolality.[17] (iv) Nanocarriers are easily decorated with specific biomarkers (peptides,[18,19] antibodies,[20,21] aptamers,[22] and so on) for active targeting.

Graphene, a two-dimensional sp^2-hybridized carbon sheet with exceptional electrical, mechanical, optical, and chemical properties, has been extensively explored for biomedical applications,[23] such as drug/gene delivery carriers,[24–26] enzyme immobilization,[27] and phototherapeutic agents.[28–31] Particularly, it has a poly-aromatic surface structure with large specific

[a]*Department of Cardiology, Xijing Hospital, The Fourth Military Medical University, Xi'an, China 710032. E-mail: wind8828@gmail.com*

[b]*Laboratory of Molecular Imaging and Nanomedicine (LOMIN), National Institute of Biomedical Imaging and Bioengineering (NIBIB), National Institutes of Health (NIH), Bethesda, MD 20892-2281, USA. E-mail: niug@mail.nih.gov; shawn.chen@nih.gov*

[c]*Research Institute of Micro/Nano Science and Technology, Shanghai Jiao Tong University, Shanghai 200240, China*

[d]*Department of Cardiovascular Surgery, Xijing Hospital, Fourth Military Medical University, Xi'an 710032, China*

[e]*Laboratory of Cellular Imaging and Macromolecular Biophysics, National Institute of Biomedical Imaging and Bioengineering (NIBIB), National Institutes of Health (NIH), Bethesda, MD 20892-2281, USA*

[f]*Center for Molecular Imaging and Translational Medicine, School of Public Health, Xiamen University, Xiamen, 361005 China*

† Electronic supplementary information (ESI) available. See DOI: 10.1039/c3nr01573d

‡ Equal contributors.

surface area, which is potentially efficient for protein loading (*e.g.* VEGF) *via* physical adsorption. Although silica nanoparticles have also been used for VEGF delivery,[10] graphene oxide (GO) nanoparticles appear to have the following advantages: (i) high loading efficiency due to two accessible surfaces of GO;[24,25] (ii) high solubility in aqueous solution;[25] and (iii) better biocompatibility.[25,28]

Herein we report the design and synthesis of multifunctional VEGF-loaded IR800-conjugated graphene oxide (GO-IR800-VEGF) for multi-modality imaging-monitored therapeutic angiogenesis of ischemic muscle. The as-prepared GO-IR800-VEGF positively targets VEGF receptors of ischemic tissues and maintains an elevated level of VEGF in ischemic tissues for a prolonged time, and finally leads to remarkable therapeutic angiogenesis.

2 Results and discussion

The synthetic route for VEGF loaded GO is illustrated in Fig. S1.† GO was prepared using flake expandable graphite as the raw material by a modified Hummers method.[28,32] Amine terminated six-arm branched PEG (10 kDa) was conjugated with GO sheets to improve their aqueous dispersibility, stability, and biocompatibility. IR800, a commonly used near-infrared (NIR) fluorescent dye, was conjugated with the amino groups of PEG to allow *in vivo* tracking of GO biodistribution by NIR fluorescence imaging. Subsequently, VEGF was loaded onto the two accessible surfaces of GO *via* physical adsorption. Fig. 1a shows the structure of GO-IR800-VEGF. The size and morphology of as-prepared GO-IR800 were characterized by atomic force microscopy (AFM). Fig. 1b shows the AFM topography image of GO-IR800 as very small sheets with a size range of 20–50 nm. The average thickness of GO-IR800, measured from the height profile of the AFM image, Fig. 1c, is about 18 nm. The thickness of a single GO sheet is ~1.2 nm. The thickness difference, ~16.8 nm, is correlated with the thickness of IR800-conjugated PEG layers covering both sides of the GO sheet.

Successful conjugation of IR800 and loading of VEGF on GO sheets were evidenced by UV-vis absorbance spectra. Fig. 1d shows the UV-vis absorbance spectra of GO, IR800, GO-IR800,

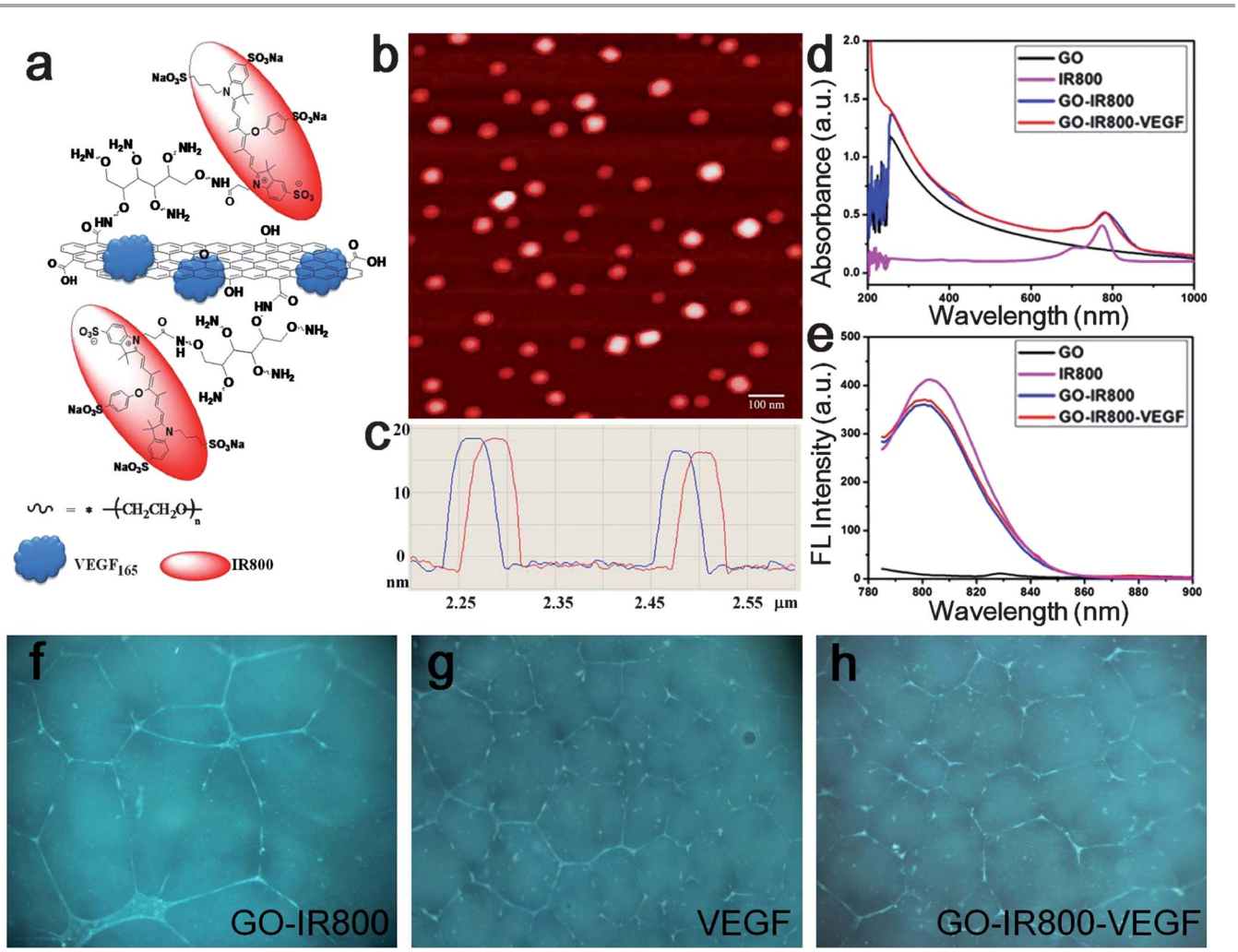

Fig. 1 (a) Schematic structure of VEGF-loaded IR800-conjugated graphene oxide (GO-IR800-VEGF). (b) Atomic force microscopy (AFM) image and (c) the height profile of GO-IR800 (scale bar, 100 nm). (d) UV-vis absorbance and (e) fluorescence emission spectra of GO, IR800, GO-IR800, and GO-IR800-VEGF. (f–h) Tube formation effects of GO-IR800 (f), free VEGF (g), and GO-IR800-VEGF and (h) on the cultured human umbilical vascular endothelial cells (HUVECs) (10 nM $VEGF_{165}$).

and GO-IR800-VEGF. The UV-vis spectrum of GO-IR800 revealed IR800 peaks superimposing with the absorption curve of GO, suggesting successful conjugation of IR800 with GO. Comparison of the spectra of GO-IR800 and GO-IR800-VEGF reveals a new shoulder peak at 280 nm, characteristic of aromatic amino acids in proteins, seen in GO-IR800-VEGF, but not in GO-IR800, IR800 or GO, suggesting the presence of VEGF protein molecules on the GO surface. The UV-vis spectrum of the VEGF protein is shown in Fig. S2.† We used excess GO to guarantee 100% loading of $VEGF_{165}$ (15 μg VEGF165 and 500 μg of GO). In this way, we did not detect any free protein (UV absorbance at 280 nm) in the removed solution after centrifugation–filtration through 100 kDa MWCO Amicon filters. Fig. 1e represents the fluorescence spectra of GO, IR800, GO-IR800, and GO-IR800-VEGF. The fluorescence emission spectra of IR800, GO-IR800, and GO-IR800-VEGF are similar to the maximum emission at ~800 nm. The samples were normalized to the same IR800 concentration (OD value) measured by UV-vis. The results also showed slight fluorescence quenching of IR800 in the GO-IR800, which is likely owing to the direct contact between IR800 and aromatic regions of the GO sheets.

After synthesis of GO-IR800-VEGF, the cellular toxicity of GO-IR800-VEGF was evaluated on MDA-MB-435 cells using MTT assay. Cell viability was normalized by the control group of cells without GO-IR800-VEGF. As shown in Fig. S3,† the results suggested a negligible cytotoxicity of GO-IR800-VEGF on MDA-MB-435 cells within the concentration range of 0–200 μg mL^{-1}. Then we tested whether VEGF preserved its pro-angiogenetic effect after loading onto GO-IR800 nanocarriers. Endothelial cells play essential roles in the angiogenic process within the skeletal muscle post-ischemia.[33] To directly investigate the effect of GO-IR800-VEGF on endothelial cells *in vitro*, we determined the effect of GO-IR800-VEGF on tube formation of human umbilical vascular endothelial cells (HUVECs). Compared with the pure GO-IR800 (Fig. 1f), GO-IR800-VEGF was able to significantly enhance tube formation to an extent similar to free VEGF treatment (10 nM $VEGF_{165}$, Fig. 1g and h). Both VEGF and GO-IR800-VEGF treated HUVEC cells developed complex mesh-like structures while GO-IR800 treated cells only form close polygons. VEGF and GO-IR800-VEGF treated cells also showed a significantly longer total capillary tube length than that of GO-IR800 ($p < 0.01$, Fig. S4†). This result indicated that the pro-angiogenic effect of VEGF on endothelial cells *in vitro* can be well preserved after loading onto GO-IR800 nanocarriers.

To assess the theranostic potential of GO-IR800-VEGF *in vivo*, we investigated its therapeutic angiogenesis effect in ischemic muscle using a well-established model of mouse hindlimb ischemia. This model is widely used for mimicking PAD and is established by ligation and excision of a section of femoral artery and all branches originated from this section of femoral artery in the right hindlimb. The sham operated left hindlimb serves as a control.[34] Low blood flow to the right hindlimb distal to the ligation site was confirmed by multiple imaging modalities (Fig. 2), including power Doppler imaging, color Doppler imaging, laser Doppler imaging (LDI), and photoacoustic (PA) imaging. Before surgery, power Doppler and color Doppler imaging in three dimensional modes displayed clear and unimpeded blood flow within femoral artery and vein and multiple branches derived from these stem vessels (Fig. 2a).

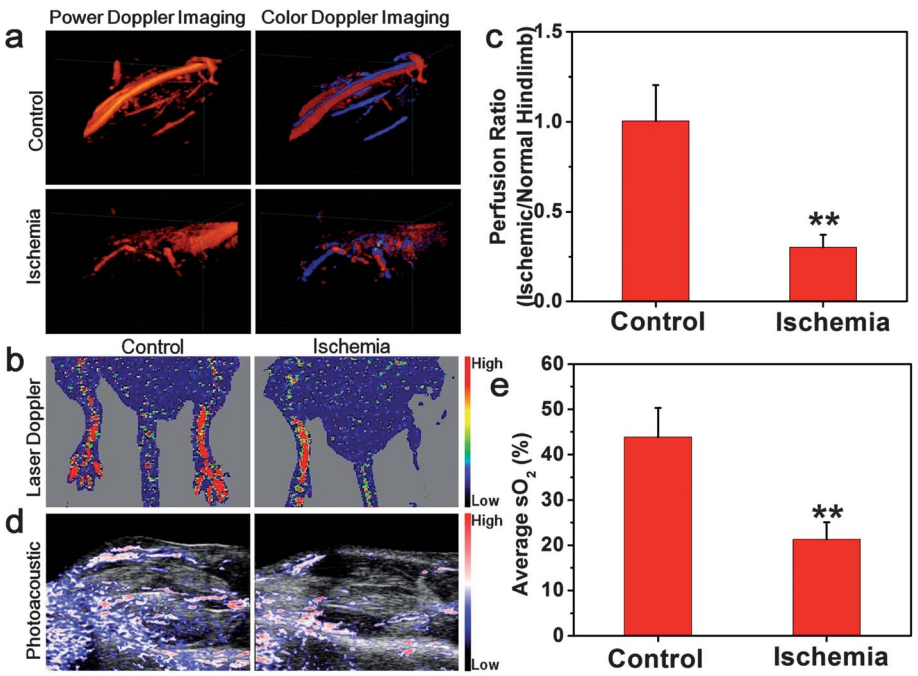

Fig. 2 Characterization of a mouse hindlimb ischemia model. (a) Three dimensional power Doppler and color Doppler images of control and ischemia groups. (b) Laser Doppler images of control and ischemia groups. (c) Quantitative analysis of tissue blood perfusion in ischemic limbs and control non-ischemic limbs (**, $P < 0.01$, as compared with the control group). (d) Photoacoustic (PA) images of the oxygen saturation (sO_2) map of control and ischemia groups. (e) Quantitative analysis of sO_2 (%) in ischemic limbs and control non-ischemic limbs (**, $P < 0.01$, as compared with the control group).

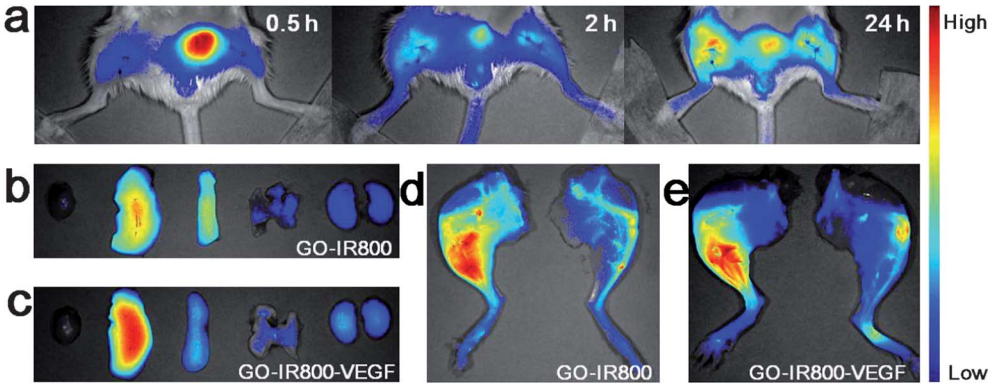

Fig. 3 Real-time *in vivo* and *ex vivo* fluorescence imaging. (a) Real-time *in vivo* NIR fluorescence images after intravenous injection of GO-IR800-VEGF in mice at different time points; (b and c) *ex vivo* NIR fluorescence images of mice tissues (from left to right: heart, liver, spleen, lung, kidneys), harvested at a 24 h time point from post-injection mice. (d) Representative fluorescent image of ischemic (left limb) and nonischemic (right limb) tissues from the mouse injected with GO-IR800. (e) Representative fluorescent images of ischemic (left limb) and nonischemic (right limb) tissues from the mouse injected with GO-IR800-VEGF.

Color Doppler imaging further distinguishes blood flow with different directions in different colors. Red and blue colors indicate the blood within vessel flows toward and away from the transducer, respectively. After ischemic injury, abrupt disruption of right femoral artery blood flow could be observed in both power Doppler and color Doppler modes with only a few traces of

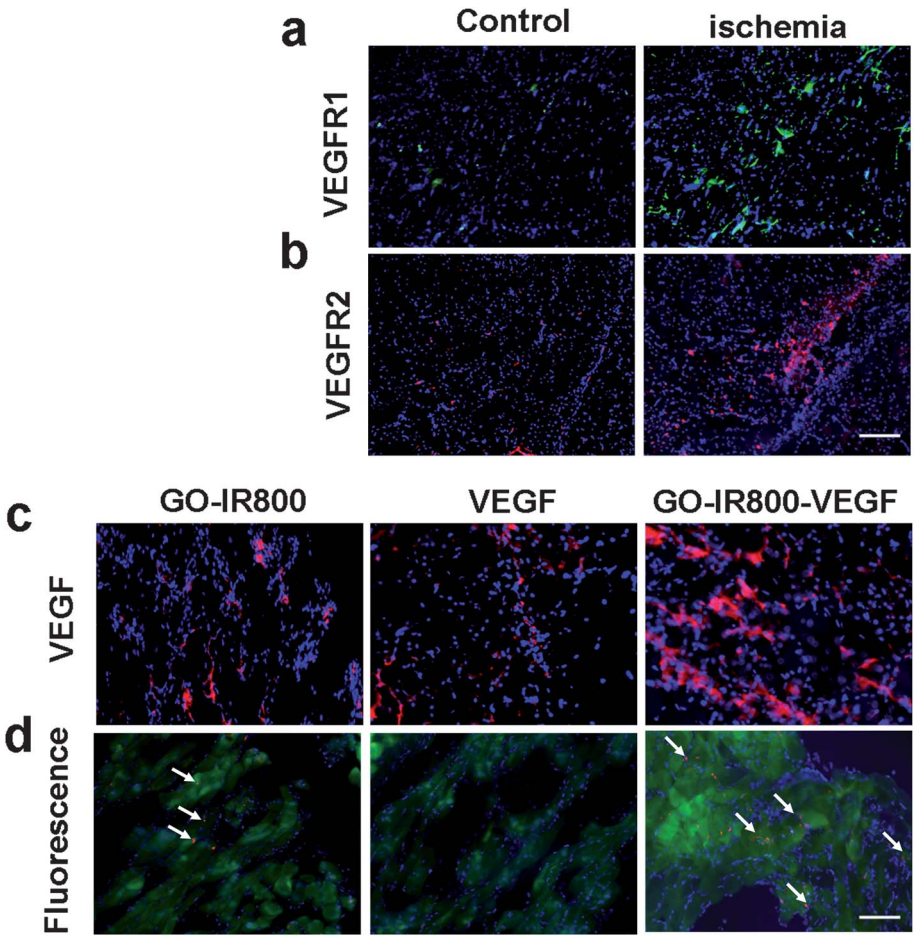

Fig. 4 Histological examination of the level of VEGFRs and VEGF in ischemic hindlimbs. (a) Immunostaining of VEGFR1 protein of cryosectioned ischemic (left) and non-ischemic (right) limbs. VEGFR1 protein is in green and nuclei were stained with 4′,6-diamidino-2-phenylindole (DAPI) and are in blue. (b) Immunostaining of VEGFR2 protein of cryosectioned ischemic (left) and non-ischemic (right) limbs. VEGFR1 protein is in red and nuclei are in blue (scale bar = 50 μm). (c) Immunostaining of VEGF protein of an ischemic limb in GO-IR800 (left), free VEGF (middle) and GO-IR800-VEGF (right) treated groups, respectively. VEGF protein is in red and nuclei are in blue. (d) Fluorescence images of the ischemic limb in GO-IR800 (left), free VEGF (middle) and GO-IR800-VEGF (right) treated groups. GO-IR800 nanoparticles are in red (arrows) and nuclei are in blue. Muscle fibers appear green due to autofluorescence (scale bar = 25 μm).

blood flow left within the muscle (Fig. 2a). Low blood perfusion in the hindlimb tissue, resulted from the ligation and excision of the right femoral artery, could also be observed using LDI (Fig. 2b), which showed that the regional blood flow was reduced to only ~20% of normal levels after ischemic surgery (1.004 ± 0.201 *vs.* 0.201 ± 0.070; $P < 0.01$). Observation of reduction in blood flow was seconded by reduction in both total and oxygenated haemoglobin content in ischemic muscle demonstrated by PA mode imaging (Fig. 2d). Oxygen saturation (sO_2) is a measure of the amount of hemoglobin binding sites occupied by oxygen and is expressed a percentage value of total binding sites (both deoxyhemoglobin and oxyhemoglobin). A low haemoglobin level resulted in low oxygen saturation (43.82 ± 6.51% *vs.* 21.28 ± 3.82%; $P < 0.01$). All these results indicate successful construction of this standard animal model of PAD.

After successful establishment of the mouse hindlimb ischemia model, we first tested whether GO-IR800-VEGF could target the ischemic hindlimb. A single dose of VEGF alone (3 μg), GO-IR800 (200 μL, 0.5 mg mL^{-1}), or GO-IR800-VEGF (200 μL, 0.5 mg mL^{-1} GO-IR800, 3 μg VEGF) was injected intravenously *via* tail vein on day 3 post-induction of the hindlimb ischemia. NIR fluorescence imaging of right ischemic and left normal hindlimbs was subsequently performed at multiple designated time points to evaluate the dynamic accumulation of GO-IR800-VEGF in an ischemic hindlimb *in vivo* (Fig. 3). The fluorescence intensity of ischemic limbs is stronger than that of non-ischemic limbs at all of the time points examined (Fig. 3a), suggesting that VEGF-loaded GO-IR800 nanocarriers could substantially target ischemic muscle. These observations could be ascribed to the increased permeability of blood vessels in hypoxic tissues, which has been confirmed by previous studies.[4,10] Ischemia in peripheral tissue leads to upregulated expression of a variety of angiogenic factors that may enhance the localized blood vessel permeability as they activate and mobilize endothelial cells in blood vessels.

To confirm the results observed *in vivo*, *ex vivo* evaluation of VEGF-loaded GO-IR800 accumulation in ischemic muscle was also performed. At 24 h time point post-injection, the mice were sacrificed and organs of GO-IR800 and GO-IR800-VEGF injected mice were harvested for *ex vivo* imaging (Fig. 3b and c). The fluorescence signal displayed in the liver could be attributed to the high uptake of GO-IR800 or GO-IR800-VEGF by the reticuloendothelial system (RES). The strong fluorescence signal in the kidneys and bladder suggests renal clearance of GO-IR800 or GO-IR800-VEGF after circulation in the bloodstream. Compared to non-ischemic hindlimbs, ischemic hindlimbs demonstrated much higher fluorescence levels, with or without

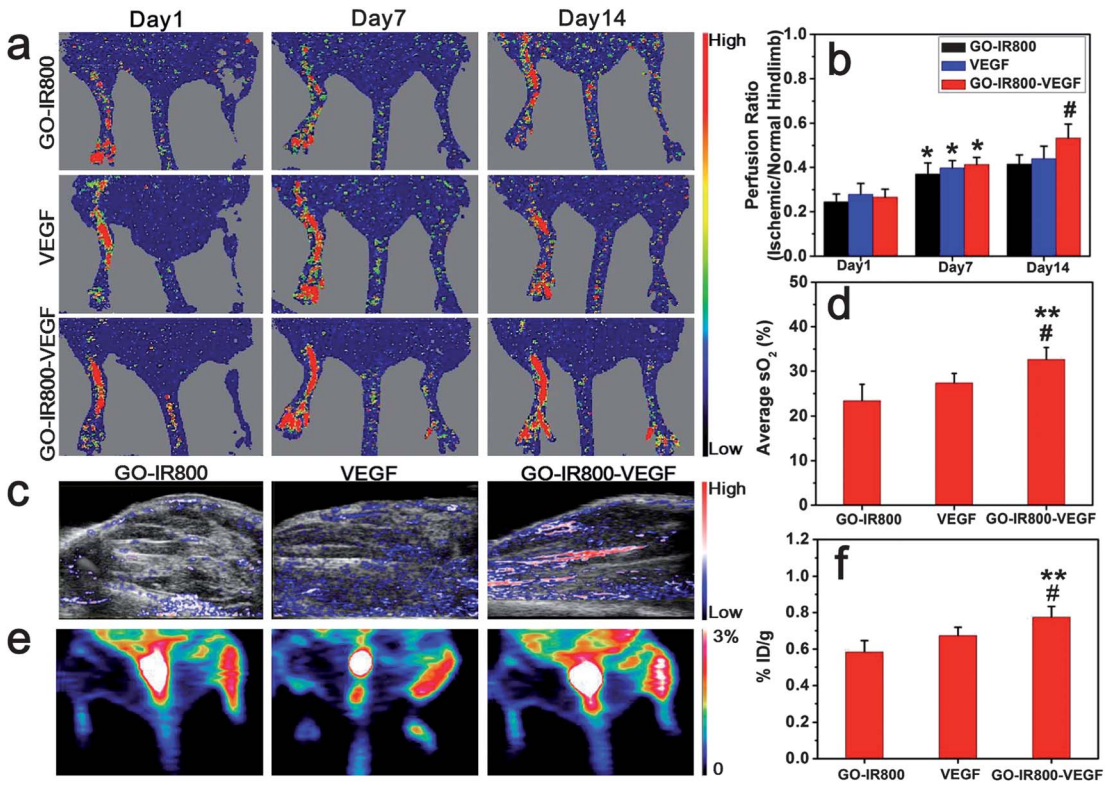

Fig. 5 Therapeutic angiogenesis of ischemic muscle. (a) Laser Doppler images of GO-IR800 (top), free VEGF (middle) and GO-IR800-VEGF (bottom) treated groups on days 1, 7 and 14 post-surgery. (b) Quantitative analysis of tissue blood perfusion in ischemic limbs and control non-ischemic limbs (*, $P < 0.05$, as compared to day 1; #, $P < 0.05$, as compared with the VEGF treated group on day 14). (c) Photoacoustic (PA) images for tissue oxygen saturation (sO_2) detection of GO-IR800 (left), free VEGF (middle) and GO-IR800-VEGF (right) treated groups on day 14 post-surgery, respectively. (d) Quantitative analysis of tissue oxygen saturation (%) within ischemic limbs of the above three groups (**, $P < 0.01$, as compared with the GO-IR800 group; #, $P < 0.05$, as compared with the free VEGF group). (e) Representative positron emission tomography (PET) images at 1 h after intravenous injection of ^{18}F-AlF-NOTA-PRGD2 (^{18}F-Alfatide) in the above three groups. (f) Quantitative analysis of tracer uptake in ischemic tissue three groups above (**, $P < 0.01$, as compared with the GO-IR800 group; #, $P < 0.05$, as compared with the free VEGF group).

loaded VEGF, which is consistent with the aforementioned *in vivo* data. Major organs of GO-IR800-VEGF treated mice were collected for histology analysis. No noticeable sign of organ damage was observed from hematoxylin and eosin (H&E) stained organ slices (see Fig. S5†), suggesting the promise of using GO-IR800-VEGF for *in vivo* applications.

Importantly, both GO-IR800 and GO-IR800-VEGF were broadly distributed throughout the entire ischemic tissue below the ligation site (Fig. 3d and e), rather than being locally centralized only surrounding the site at which femoral artery was blocked. The observed even and extensive distribution of nanocarriers in a large area of ischemic tissue suggests that therapeutic molecules delivered by GO are able to reach a large volume of targeted tissue. Interestingly, the relative fluorescence ratio of ischemic limbs to non-ischemic limbs in the GO-IR800-VEGF treated group was found to be much higher than that of the GO-IR800 treated group (3.39 *vs.* 1.84) (see Fig. S6†), suggesting that VEGF itself might also play a role in the accumulation of GO-IR800-VEGF in ischemic tissue, mostly likely due to the up-regulation of VEGF receptors in the ischemic tissue induced by hypoxia. Thus, VEGF might function as both a guiding agent and a therapeutic drug. This hypothesis was also supported by *ex vivo* histological evaluation for VEGF receptor (VEGFR) expression and local VEGF level. Immunostaining demonstrated up-regulated expression of both VEGFR1 and VEGFR2 in an ischemic region compared with a non-ischemic region (Fig. 4a and b). Meanwhile, an enhanced level of VEGF in the ischemic muscle derived from GO-IR800-VEGF treated mice could also be detected by immunostaining (Fig. 4c). Furthermore, fluorescence images of cryosectioned ischemic limbs also indicate a significant increase in deposition of nanocarriers in ischemic muscle fibers after GO-IR800-VEGF injection, as compared to both non-ischemic tissue and ischemic tissue derived from GO-IR800 treated mice (Fig. 4d).

To assess the angiogenic response to intravenous injection of GO-IR800-VEGF, multiple imaging modalities were used to evaluate the therapeutic effect. Firstly, LDI at various time points was performed to monitor the blood perfusion in hindlimbs. On day 1 post-induction of ischemia, the regional blood flow in ischemic limbs was abruptly decreased to approximately 20% of normal limbs in all groups after ischemic surgery as expected (Fig. 5a). The untreated group showed a slow increase in blood flow from 20% to 40% of normal values over time, mainly due to the spontaneous recovery induced by endogenous capillary formation and the sprouting of collateral arteries,[35] a similar extent of blood flow recovery was observed in the GO-IR800 treated group. Administration of free VEGF, mimicking the routine delivery approach, resulted in no significant difference from the GO-IR800 treatment control group. Nonetheless, GO-IR800-VEGF led to much better

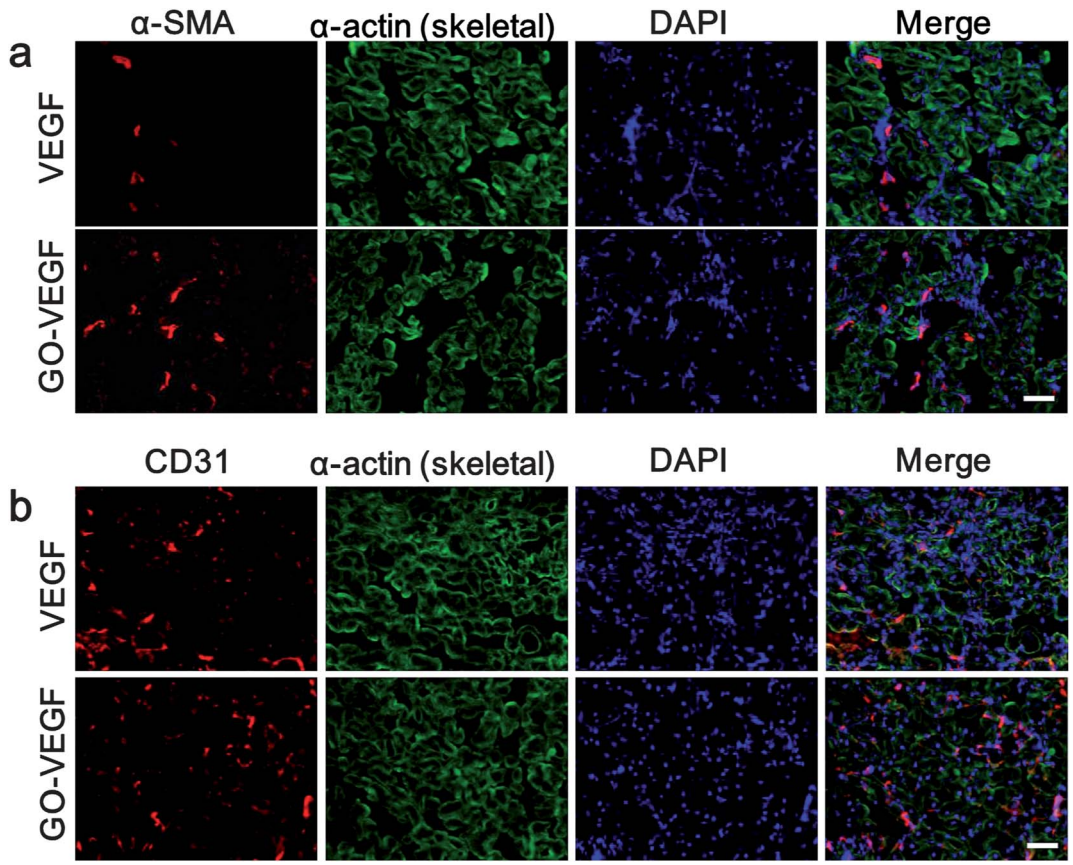

Fig. 6 Histological confirmation of therapeutic angiogenesis. (a) Immunostaining of CD31 protein of the cryosectioned ischemic limb in free VEGF and GO-IR800-VEGF treated groups on day 9 post-surgery, respectively. (b) Immunostaining of α-SMA protein of a cryosectioned ischemic limb in two groups above on day 14 post-surgery. CD31 protein is in red, α-actin protein is in green and nuclei are in blue (scale bar = 25 μm).

recovery of blood perfusion over entire 14 days and reached nearly 60% of the non-ischemic tissue (Fig. 5b), a 1.5-fold increase as compared to the other conditions at the end point of this study.

In addition, PA mode imaging was used to detect the regional oxygen saturation in ischemic tissue. Oxygen saturation serves as an important index to monitor functional angiogenesis. GO-IR800-VEGF treatment was capable of significantly increasing oxygen supply to ischemic muscle, as evidenced by the much stronger signal intensity observed in the GO-IR800-VEGF treated group 2 weeks post-surgery, as compared to the other groups (Fig. 5c and d). The elevated oxygen delivery is most likely attributed to the enhanced capillary formation and small artery sprouting within ischemic tissue by GO-IR800-VEGF treatment. This result of increased oxygen saturation suggests that increased angiogenesis by GO-IR800-VEGF treatment can be translated into elevation of oxygen supply to ischemic tissue, which, in turn, enhances the survival and function of the ischemic hindlimb.

Integrins, a family of proteins, have been well documented on their impact in cellular adhesion and migration into the extracellular matrix (ECM).[36] Among this family, $\alpha_v\beta_3$ integrin is highly expressed on activated neovascular endothelial cells and plays an essential role in endothelial cell survival and migration during angiogenesis.[37] Therefore, integrin $\alpha_v\beta_3$ is able to function as a target for angiogenesis imaging with the specific probes.[38–40] In terms of good imaging qualities and convenient synthesis, ^{18}F-AlF-NOTA-PRGD2 (^{18}F-Alfatide) has been reported to be a promising tracer for PET imaging of integrin $\alpha_v\beta_3$ expression.[41–43]

In the present study, static PET imaging was also performed 1 week post-treatment to evaluate angiogenesis using ^{18}F-Alfatide as the imaging probe. Fig. 5e shows representative coronal PET images of mouse hindlimbs at 1 h post injection of ^{18}F-Alfatide (100 μCi per mouse). Based on PET quantification (Fig. 5f), the ischemic tissue uptake of ^{18}F-Alfatide after GO-IR800-VEGF treatment (0.77 ± 0.06%ID per g) is significantly higher than that in the GO-IR800 group (0.56 ± 0.05%ID per g; $P < 0.01$) and the VEGF treatment group (0.67 ± 0.05%ID per g; $P < 0.05$), suggesting the strong therapeutic angiogenesis effect of GO-IR800-VEGF.

The pro-angiogenetic effect of GO-IR800-VEGF treatment was confirmed by quantification of blood vessel densities using immunostaining of CD31 (marker for endothelial cell) and α-SMA (marker for small arteriole). As shown in Fig. 6, GO-IR800-VEGF treatment dramatically increased CD31 (Fig. 6a) and α-SMA (Fig. 6b) expression levels over VEGF treatment. The upregulation of both CD31 and α-SMA suggests the increased density of both capillaries and small arterioles.

3 Experimental section

Synthesis of PEG-modified graphene oxide

Graphene oxide (GO) was prepared using flake expandable graphite as the raw material by a modified Hummers method. To prepare PEG-modified GO, 5 mL of GO aqueous suspension (~3 mg mL^{-1}) was sonicated for ~30 min. Then NaOH (0.12 g mL^{-1}) was added to the GO suspension under sonication for another 3 h. The resulting solution was neutralized, purified, and separated by repeated rinsing and filtration, then a solution of 6-arm-polyethylene glycol-amine (Sunbio Inc.) (3 mg mL^{-1}) was added to the GO solution (0.5 mg mL^{-1}) and the mixture was sonicated for 5 min. *N*-(3-Dimethylaminopropyl-*N*′-ethyl-carbodiimide) hydrochloride (EDC, from Fluka Inc.) was then added to the mixture in two equal portions to give a final concentration of 1 mg mL^{-1}. The reaction was allowed to stand overnight, yielding a PEG-modified GO solution which was stored at 4 °C for further use.

Synthesis of VEGF-loaded IR800-conjugated graphene oxide (GO-IR800-VEGF)

The excess PEG in the as-synthesized PEG-modified GO sample was removed by Amicon centrifugal filters (Millipore) with 100 kDa molecular weight cut off (MWCO) and washed with water several times. The purified PEG-modified GO (0.5 mg mL^{-1}) was reacted with an amine reactive dye, IR800 (LI-COR Biosciences) at 0.1 mg mL^{-1} in a pH 7.5 phosphate buffer (0.02 M). The reaction was allowed to stand overnight at room temperature in the dark. The excess dye was removed by centrifugation filtration through 100 kDa MWCO Amicon filters and washed with water 8× until no IR800 could be detected in the supernatant by UV-vis spectroscopy.

Recombinant mouse vascular endothelial growth factor-165 (VEGF-A or VEGF-165) is a nonglycosylated, disulfide-linked homodimer, containing 165 amino acids with a molecular mass of 39 kDa. VEGF-165 was purchased from Shenandoah Biotechnology, Inc. 1 mL of 0.5 mg mL^{-1} GO-IR800 in PBS buffer (pH = 7.4) was mixed with 15 μg VEGF-165 and shaken overnight at 4 °C. Excess VEGF-165 were removed by centrifugation filtration through 100 kDa MWCO Amicon filters and washed away with PBS buffer (pH = 7.4) several times. GO-IR800-VEGF retained in the filter was washed 4 to 6 times and re-suspended in PBS buffer (pH = 7.4). The formed GO-IR800-VEGF was stored at 4 °C.

Characterization

Briefly, AFM imaging of the samples was carried out under a range of deposition conditions in fluid, rinsed with deionized water and dried under a gentle flow of N_2 or Ar gas, using gentle tapping-mode and mostly with a PicoForce Multimode AFM (Bruker, CA) consisting of a Nanoscope® V controller, a type E scanner head, and a sharpened TESP-SS (Bruker, CA), or a similar AFM cantilever. For GO-IR800 sample visualization, suitable surface attachment of the respective sample was achieved readily by 5 min incubation of 5 μL of 6 μg mL^{-1} fluid suspension on freshly peeled and slightly tilted mica on metal disks of 12 mm diameters. The excess fluid was blown away by an inert gas gush, followed by a complete drying of the sample surface under gentler gas flow. The sample was then sealed into the instrument compartment dehumidified by Drierite® particles and imaged *via* standard optimizations and a range of imaging settings to enhance reliability. For fuller comparison, the sample surfaces were often rinsed up to 2 times each with

30–50 μL of deionized water to remove salt deposits, dried under gentle air flow, and re-imaged similarly. AFM images were evaluated within the Nanoscope software (version 7.3, Bruker, CA), and exported to Image J (version 1.4x, NIH, Bethesda, MD) for further analyses and display.

UV-vis spectra were recorded at 20 °C using a Genesys 10S UV-vis spectrophotometer (Thermo Scientific, Waltham, MA) equipped with a 10 mm quartz cell, where the light path length was 1 cm. Fluorescence spectra were recorded on a Hitachi F-7000 spectrofluorimeter (HITACHIH, Japan).

Tube formation assay

100 μL of Matrigel (growth factor reduced, BD Biosciences) was added to each well of a 48-well plate, and polymerized at 37 °C for 1 hour. HUVECs (1×10^4) were seeded onto Matrigel, in endothelial cell basal medium-2 with EGM-2 Bullet Kit. After 1 hour culture, GO-IR800-VEGF, GO-IR800 or VEGF (10 nM) was added.

Animals

All experiments were performed in adherence with the National Institutes of Health guidelines on the use of laboratory animals and were approved by the National Institutes of Health Committee on Animal Care.

Mice hindlimb model

Hindlimb ischemia was achieved by right femoral artery excision as previously described.[44] In brief, ischemia was induced by ligation and segmental resection of the femoral vessels proximal to the bifurcation with silk sutures (#7.0). A sham operation was performed in the left hindlimb without ligation and excision of the femoral artery, such that the right hindlimb is ischemic and the contralateral left hindlimb serves as a control. Hindlimb muscles such as tibialis anterior (TA), extensor digitorum longus, gastrocnemius, soleus, and plantaris were harvested at various time points after the induction of ischemia and processed for histological examination. All the measurements were performed in contralateral and ischemic muscles of the hind limbs.

Real-time acquisition of NIR fluorescence images *in vivo*

Optical data acquisition and analysis were done using DyCE function in Maestro 2.0 *in vivo* imaging system (Cambridge Research & Instrumentation, Woburn, MA). 0.3 μg VEGF or the same concentration of VEGF loaded with GO-IR800 or an equal amount of GO-IR800 alone in 100 μl PBS were each injected *via* tail vein into Balb/c mice ($n = 5$) on day 2 post-hindlimb ischemia surgery. After 0.5, 1, 2, 4, 6 and 24 h post-injection, the mice were subjected to *in vivo* real-time optical imaging by Maestro 2.0 configured for NIR detection. During the injection and image acquisition process, the mice were anesthetized with 1.0–2.0% isoflurane in oxygen delivered at a flow rate of 1.0 L min^{-1}. After completion of the image acquisition, spectral unmixing yielded the pseudocolored images of the pure spectrum of ZW-1. Image pre-processing and analysis were performed using the DyCE software provided by the manufacturer. For quantitative comparison, regions of interest (ROIs) were drawn over ischemic and non-ischemic hindlimbs, and the average signal ($\times 10^6$ photons per cm^2 per s) for each area was measured. Results were presented as mean ± S.D.

Small animal PET imaging

In the 1st week after hindlimb ischemia surgery, PET imaging scans were performed using an Inveon microPET scanner (Siemens Preclinical Solutions). Balb/c mice of different groups were anesthetized with 1.0–2.0% isoflurane in oxygen delivered at a flow rate of 1.0 L min^{-1} and approximately 3.75 MBq (100 μCi) of ^{18}F-AlF-NOTA-PRGD2 (^{18}F-Alfatide) was administered *via* tail vein injection. Ten minutes static PET images were acquired at 1 h after injection of the tracer.

The images were reconstructed by a three-dimensional ordered subsets expectation maximization (3D-OSEM) algorithm, and no correction was applied for attenuation or scatter. Image analysis was done using ASI Pro VMTM software. The total RGD uptake (%ID per g) of the ischemic hindlimb tissue was determined by drawing three-dimensional regions of interest (ROIs) surrounding an entire limb on the coronal images. The radioactivity contained in the ROI divided by the dose administered to the animal gave the %ID per g. Each group contained 4–5 mice.

Power Doppler and color Doppler scans of hindlimbs

Before and 1 day post-hindlimb ischemia surgery, power Doppler and color Doppler scans were performed using a Vevo 2100 Imaging System (VisualSonics Vevo 2100, Toronto, ON, Canada). After Balb/c mice were anesthetized with 1.0–2.0% isoflurane in oxygen delivered at a flow rate of 1.0 L min^{-1}, flow velocity and spatial vascular profile in the right hindlimb were evaluated by power Doppler with a 32 MHz linear transducer in three-dimensional mode. Percent vascularity, an index of relative vascular density, was calculated by measurement tools in the power Doppler mode to assess the vascularity of the hindlimb. Color Doppler mode in three-dimension was also used to provide a visual overview of flow within the normal and ischemic skeletal muscle tissue as well as delineate the flow direction and velocity by red and blue color spectrums. Small vessels, which cannot be detected in B-mode, are able to be rapidly identified by color Doppler mode.

Oxygen supply assessments by photoacoustic (PA) mode scan

Before, 1 day, and 14 days post-surgery, (PA) mode scans were performed based on a Vevo LAZR platform (VisualSonics Vevo LAZR, Toronto, ON, Canada). After Balb/c mice were anesthetized with 1.0–2.0% isoflurane in oxygen delivered at a constant flow rate of 1.0 L min^{-1}, oxygenated hemoglobin and total hemoglobin within the vessel of the hindlimb were detected by PA mode scan with 700/750 nm wavelength and these functional hemodynamic results can be visually overlaid with anatomical images. Hemoglobin content and quantification and oxygen saturation calculation and quantification were measured by HemoMeaZure™ Tool and OxyZated™ Tool,

respectively. Oxygen saturation (sO_2%) was calculated as the percent of oxygenated hemoglobin in total hemoglobin in the same regions of interest (ROI) to indicate the oxygen supply to the hindlimb at different time points.

Immunofluorescence staining

Mouse skeletal muscles within the ischemic hindlimb 14 days after surgery were harvested for immunofluorescence staining. After the sample was embedded in O.C.T. and snap-frozen on dry ice, serial cryosections (10 μm thickness) were cut and mounted on glass slides (Fisher, Pittsburgh, PA, USA). After drying at room temperature, slides were fixed with 4% paraformaldehyde in PBS for 10 min and later incubated with 1% bovine serum albumin (BSA; Sigma) in PBS.

For single antibody staining, slides were incubated with rabbit anti-VEGFR2 (diluted 1 : 150; Abcam, Cambridge, MA, USA), mouse anti-VEGF (diluted 1 : 150; Abcam, Cambridge, MA, USA) or mouse anti-VEGFR1 (diluted 1 : 200; Abcam, Cambridge, MA, USA). The combinations were visualized using a Cy3-conjugated anti-rabbit (Sigma) or fluorescein isothiocyanate (FITC)-conjugated anti-mouse (Sigma) secondary antibodies.

For double antibodies staining, slides were incubated with rabbit anti-CD31 (diluted 1:200; Abcam, Cambridge, MA, USA) or rabbit anti-alpha-smooth muscle actin (α-SMA) (diluted 1:150; Abcam, Cambridge, MA, USA) mixed with mouse anti-α-actin (skeletal) primary antibodies solution (diluted 1:250; Abcam, Cambridge, MA, USA), respectively. The combinations were visualized using a mixture of Cy3-conjugated anti-rabbit (Sigma) and fluorescein isothiocyanate (FITC)-conjugated anti-mouse (Sigma) secondary antibodies.

Statistical analysis

Results were presented as mean ± S.D. Two-tailed paired and unpaired Student's *t*-tests were used to determine differences within groups and between groups, respectively. P value <0.05 was considered statistically significant.

4 Conclusions

In summary, VEGF-loaded IR800-conjugated graphene oxide (GO-IR800-VEGF) specifically and efficiently targets ischemic muscle tissues in the murine hindlimb ischemia model. Both active and passive targeting of GO-IR800-VEGF led to a high local VEGF concentration in the ischemic tissue. The *in vivo* pharmacokinetics and biodistribution of GO-IR800-VEGF was successfully monitored by NIR fluorescence imaging. The therapeutic angiogenesis of ischemic muscle was confirmed by multiple imaging modalities including LDI, PA, and PET imaging, which were further validated by *ex vivo* immunostaining of CD31 and α-SMA. Although more efforts are required to further understand the *in vivo* behaviors and the long-term toxicology of GO, our work demonstrates the success of using GO for efficient VEGF delivery *in vivo* by intravenous administration and suggests the great promise of using graphene oxide in theranostic applications for treating ischemic disease.

Acknowledgements

This work was supported by the National Key Basic Research Program (973 Project) (2010CB933901, 2012CB518101 and 2013CB733802), the National Science Foundation of China (81272987, 31170961, 51102258, 81090274 and 81227901), Zhejiang Province Foundation (LY12H11011), the Intramural Research Program (IRP) of the National Institute of Biomedical Imaging and Bioengineering (NIBIB) and National Institutes of Health (NIH).

References

1 K. Ouriel, *Lancet*, 2001, **358**, 1257–1264.
2 J. D. Hooi, H. Stoffers, J. A. Knottnerus and J. Van Ree, *Br. J. Gen. Pract.*, 1999, **49**, 49–55.
3 J. Tongers, J. Roncalli and D. Losordo, *Circulation*, 2008, **118**, 58–65.
4 N. Bhise, R. Shmueli, J. Sunshine, S. Tzeng and J. Green, *Expert Opin. Drug Delivery*, 2011, **8**, 485–504.
5 L. Deveza, J. Choi and F. Yang, *Theranostics*, 2012, **2**, 801–814.
6 M. Giacca and S. Zacchigna, *Gene Ther.*, 2012, **19**, 622–629.
7 L. Diaz-Sandoval and D. Losordo, *Expert Opin. Biol. Ther.*, 2003, **3**, 599–616.
8 H. Park, F. Yang and S. Cho, *Adv. Drug Delivery Rev.*, 2012, **64**, 40–52.
9 M. J. Webber, J. Tongers, C. J. Newcomb, K.-T. Marquardt, J. Bauersachs, D. W. Losordo and S. I. Stupp, *Proc. Natl. Acad. Sci. U. S. A.*, 2011, **108**, 13438–13443.
10 J. Kim, L. Cao, D. Shvartsman, E. A. Silva and D. J. Mooney, *Nano Lett.*, 2011, **11**, 694–700.
11 M. Simons, B. Annex, R. Laham, N. Kleiman, T. Henry, H. Dauerman, J. Udelson, E. Gervino, M. Pike and M. Whitehouse, *Circulation*, 2002, **105**, 788–793.
12 T. Henry, B. Annex, G. McKendall, M. Azrin, J. Lopez, F. Giordano, P. Shah, J. Willerson, R. Benza and D. Berman, *Circulation*, 2003, **107**, 1359–1365.
13 R. Lederman, F. Mendelsohn, R. Anderson, J. Saucedo, A. Tenaglia, J. Hermiller, W. Hillegass, K. Rocha-Singh, T. Moon and M. Whitehouse, *Lancet*, 2002, **359**, 2053–2058.
14 P. Huang, Z. Li, J. Lin, D. Yang, G. Gao, C. Xu, L. Bao, C. Zhang, K. Wang and H. Song, *Biomaterials*, 2011, **32**, 3447–3458.
15 T. Kishino, H. Hoshikawa, Y. Nishiyama, Y. Yamamoto and N. Mori, *J. Nucl. Med.*, 2012, **53**, 1521–1527.
16 P. Huang, J. Lin, X. Wang, Z. Wang, C. Zhang, M. He, K. Wang, F. Chen, Z. Li, G. Shen, D. Cui and X. Chen, *Adv. Mater.*, 2012, **24**, 5104–5110.
17 J. Hainfeld, F. Dilmanian, D. Slatkin and H. Smilowitz, *J. Pharm. Pharmacol.*, 2008, **60**, 977–985.
18 Z. Li, P. Huang, X. Zhang, J. Lin, S. Yang, B. Liu, F. Gao, P. Xi, Q. Ren and D. Cui, *Mol. Pharm.*, 2010, **7**, 94–104.
19 Z. Li, P. Huang, J. Lin, R. He, B. Liu, X. Zhang, S. Yang, P. Xi, Q. Ren and D. Cui, *J. Nanosci. Nanotechnol.*, 2010, **10**, 4859–4867.
20 C. W. Kessinger, O. Togao, C. Khemtong, G. Huang, M. Takahashi and J. Gao, *Theranostics*, 2011, **1**, 263–273.

21 P. Huang, L. Bao, D. Yang, G. Gao, J. Lin, Z. Li, C. Zhang and D. Cui, *Chem.–Asian J.*, 2011, **6**, 1156–1162.
22 Z. Li, P. Huang, R. He, J. Lin, S. Yang, X. Zhang, Q. Ren and D. Cui, *Mater. Lett.*, 2010, **64**, 375–378.
23 H. Shen, L. Zhang, M. Liu and Z. Zhang, *Theranostics*, 2012, **2**, 283–294.
24 P. Huang, C. Xu, J. Lin, C. Wang, X. Wang, C. Zhang, X. Zhou, S. Guo and D. Cui, *Theranostics*, 2011, **1**, 240–250.
25 Z. Liu, J. T. Robinson, X. Sun and H. Dai, *J. Am. Chem. Soc.*, 2008, **130**, 10876–10877.
26 Z. Liu and X. Liang, *Theranostics*, 2012, **2**, 235–237.
27 J. Zhang, F. Zhang, H. Yang, X. Huang, H. Liu and S. Guo, *Langmuir*, 2010, **26**, 6083–6085.
28 K. Yang, S. Zhang, G. Zhang, X. Sun, S.-T. Lee and Z. Liu, *Nano Lett.*, 2010, **10**, 3318–3323.
29 L. Cao, S. T. Yang, X. Wang, P. G. Luo, J. H. Liu, S. Sahu, Y. Liu and Y. P. Sun, *Theranostics*, 2012, **2**, 295–301.
30 K. Yang, L. Hu, X. Ma, S. Ye, L. Cheng, X. Shi, C. Li, Y. Li and Z. Liu, *Adv. Mater.*, 2012, **24**, 1868–1872.
31 J. T. Robinson, S. M. Tabakman, Y. Liang, H. Wang, H. Sanchez Casalongue, D. Vinh and H. Dai, *J. Am. Chem. Soc.*, 2011, **133**, 6825–6831.
32 W. S. Hummers Jr and R. E. Offeman, *J. Am. Chem. Soc.*, 1958, **80**, 1339.
33 E. Chavakis and S. Dimmeler, *Arterioscler., Thromb., Vasc. Biol.*, 2002, **22**, 887–893.
34 T. Couffinhal, M. Silver, L. P. Zheng, M. Kearney, B. Witzenbichler and J. M. Isner, *Am. J. Pathol.*, 1998, **152**, 1667–1679.
35 A. Limbourg, T. Korff, L. C. Napp, W. Schaper, H. Drexler and F. P. Limbourg, *Nat. Protocols*, 2009, **4**, 1737–1748.
36 G. Niu and X. Chen, *Theranostics*, 2011, **1**, 30–47.
37 P. C. Brooks, R. Clark and D. A. Cheresh, *Science*, 1994, **264**, 569–571.
38 W. Cai, G. Niu and X. Chen, *Curr. Pharm. Des.*, 2008, **14**, 2943–2973.
39 Z. Li, Q. Jin, C. Huang, S. Dasa, L. Chen, L. Yap, S. Liu, H. Cai, R. Park and P. S. Conti, *Theranostics*, 2011, **1**, 371–380.
40 L. Zhu, N. Guo, Q. Li, Y. Ma, O. Jacboson, S. Lee, H. S. Choi, J. R. Mansfield, G. Niu and X. Chen, *Theranostics*, 2012, **2**, 746–756.
41 L. Lang, W. Li, N. Guo, Y. Ma, L. Zhu, D. O. Kiesewetter, B. Shen, G. Niu and X. Chen, *Bioconjugate Chem.*, 2011, **22**, 2415–2422.
42 H. Gao, L. Lang, N. Guo, F. Cao, Q. Quan, S. Hu, D. O. Kiesewetter, G. Niu and X. Chen, *Eur. J. Nucl. Med. Mol. Imaging*, 2012, **39**, 683–692.
43 W. Wan, N. Guo, D. Pan, C. Yu, Y. Weng, S. Luo, H. Ding, Y. Xu, L. Wang, L. Lang, Q. Xie, M. Yang and X. Chen, *J. Nucl. Med.*, 2013, **54**, 691–698.
44 A. Matsakas, V. Yadav, S. Lorca, R. M. Evans and V. A. Narkar, *Circ. Res.*, 2012, **110**, 1087–1096.